DEVELOPMENT OF REGIONAL PHASE TOMOGRAPHIC ATTENUATION MODELS FOR EURASIA

Thorne Lay[1], Xiao-Bi Xie[1], Xiaoning (David) Yang[2], and Marie D. Arrowsmith[2]

University of California, Santa Cruz[1] and Los Alamos National Laboratory[2]

ABSTRACT

We are developing regional-phase (Pn, Pg, Sn, Lg) tomographic attenuation models for Eurasia. The models will be integrated into the National Nuclear Security Administration (NNSA) Knowledge Base and used in the Magnitude and Distance Amplitude Correction (MDAC) station calibration for the development of regional seismic discriminants. Our current focus is on Pn, an extremely important phase in seismic event identification.

Accurately accounting for regional-phase geometric spreading is critical for the development of useful attenuation models. It is particularly important for Pn and Sn waves because the propagation mode of these waves makes them more susceptible to upper mantle velocity structures and the Earth's sphericity, which in turn causes the geometric spreading of Pn (and Sn) to be dependent on frequency as well as on range in a complicated way. We conduct numerical simulations to quantify P_n and S_n geometric spreading in a spherical Earth model with constant mantle velocities. Based on our simulation results, we present new P_n and S_n geometric spreading models in the forms

$$G(r,f) = [10^{n_3(f)}/r_0](r_0/r)^{n_1(f)\log(r_0/r)+n_2(f)} \text{ and } n_i(f) = n_{i1}\left[\log(f/f_0)\right]^2 + n_{i2}\log(f/f_0) + n_{i3},$$

where i = 1, 2 or 3. r is epicentral distance; f is frequency; r_0 = 1 km and f_0 = 1 Hz. We derive values of coefficients n_{ij} by fitting the model to computed P_n and S_n amplitudes for a spherical Earth model having a 40-km-thick crust, generic values of P and S velocities and a constant-velocity uppermost mantle.

We apply the new spreading model to observed data in Eurasia to estimate average P_n attenuation, obtaining more reasonable results compared to using the standard power-law model. Our new P_n and S_n geometric-spreading models provide generally applicable reference behavior for spherical Earth models with constant uppermost-mantle velocities. Since our region of interest encompasses most of Eurasia from the Equator to the North Pole, simple regular gridding methods such as dividing the region with latitude and longitude lines would result in cells with drastically different cell sizes for the tomographic inversion. To avoid this problem and to optimize the resolution of the tomographic model based on data distribution, we have implemented several gridding schemes. They include equal-cell-size gridding and variable-cell-size gridding based on certain criteria such as the number of path hits. These gridding schemes will be tested in future tomographic inversions to find an optimum gridding method.

To prepare for the attenuation tomographic inversion, we have been collecting and measuring regional-phase amplitude data from the Incorporated Research Institute for Seismology Data Management Center and from the Los Alamos National Laboratory Ground-Based Nuclear Explosion Monitoring Research and Engineering program database. Initial Pn amplitude measurements exhibit similar decay behavior as what we see in the synthetic data. To improve our data coverage, we are conducting further data collection, phase picking and amplitude measurement.

OBJECTIVE

The objective of this project is to develop 1-Hz, two-dimensional, regional-phase (*Pn, Pg, Sn* and *Lg*) tomographic attenuation models for Eurasia. The models will be used in MDAC for improved event identification.

RESEARCH ACCOMPLISHED

Pn geometric spreading

Accurately accounting for geometric spreading is critical for the development of meaningful regional-phase attenuation models. This is particularly true for *Pn* and *Sn* waves because the nature of their wave propagation renders them acutely sensitive to upper mantle velocity structure and the Earth's sphericity. Even simple one-dimensional (1D) velocity models can produce geometric spreading of *Pn* and *Sn* that is strongly dependent on frequency and range (e.g., Sereno and Given, 1990). If frequency dependence of the geometric spreading actually occurs and is neglected, the attenuation model will acquire incorrect frequency dependence. Similar arrival times of *Pg* and *Pn* phases and *Pn* and *P* phases at their respective crossover distances result in rapidly changing *P*-wave amplitudes, difficulty in phase isolation and identification, and uncertainty in appropriate specification of the propagation path and geometric spreading at these distances. Lateral variation of Moho topography and upper-mantle lid velocity and fine scale heterogeneity of the lower crust and/or mantle lid further introduce 2D and 3D complexities into *Pn* and *Sn* spreading.

We conduct most of our simulations using the reflectivity method. Results from reflectivity calculations are compared with results calculated with a 2D finite-difference code (Xie and Lay, 1994) and a 2.5D axisymmetric spherical finite-difference code, SHaxi, to confirm that the earth flattening transform (EFT) and layer discretization required by the reflectivity method do not produce numerical artifacts. The reflectivity method generates complete synthetic seismograms within a specified slowness range for 1D, plane-layered velocity models. In order to use the reflectivity method for a spherically symmetric Earth model, we apply the EFT to transform the spherical Earth model to a plane Earth model. Transformations of velocity *v* and depth *z* are (Chapman, 1973; Müller, 1977)

$$v_f = \frac{R}{R-z_r} v_r \quad \text{and} \quad z_f = R \ln\left(\frac{R}{R-z_r}\right), \tag{1}$$

where *R* is the radius of the Earth. Subscript *r* designates values in the spherical (radially symmetric) model and subscript *f* designates values in the plane (flat) model. The density ρ transformation is

$$\rho_f = \left(\frac{R}{R-z_r}\right)^m \rho_r, \tag{2}$$

which is not unique since *m* can take any value between -5 and 1. For regional body-waves, the choice of *m* is not critical (Müller, 1977). We choose *m* = -1 for *P/SV* simulations (Müller, 1977) and *m* = -5 for *SH* simulations (Chapman, 1973). We experimented with different values of *m* and the results were basically unchanged. Finally the transformation of amplitudes calculated from plane-model simulations back to corresponding amplitudes in the spherical model is

$$A_r = \left(\frac{\Delta}{\sin\Delta}\right)^{1/2} \left(\frac{R}{R-Z_r}\right)^{\frac{m+5}{2}} A_f, \tag{3}$$

where Z_r is the depth of the source in the spherical model and Δ is epicentral distance in radians.

We approximate the velocity gradient resulting from the EFT (Equations 1 and 2) with homogeneous layers in the plane Earth model, as is required by the reflectivity method. The thickness of these layers affects the accuracy of the approximation, with thinner layers yielding more accurate results. We set the thickness of these layers to be about 0.4 of the minimum wavelength of the waves to be modeled, which appears to be more than adequate. Further reducing the ratio (e.g., from 0.4 to 0.2 of the minimum wavelength) does not alter the results appreciably. The total thickness of the gradient zone is set to be more than 100 km larger than the maximum penetration depth of the direct wave in a homogeneous spherical model recorded at the longest epicentral distance considered. This thickness guarantees that no P_n or S_n waves observed within the distance range of interest are affected by the lower boundary of the gradient zone. Below the gradient zone, the velocity is constant.

We use the same generic spherical Earth model considered by Sereno and Given (1990) as the base model for our simulations and use the synthetics from the simulation to derive parameters of the P_n and S_n geometric-spreading models that we develop. The reference Earth model consists of a 40-km-thick outer layer, representative of an average continental crust, with a constant-velocity mantle underneath (Figure 1). The model has no anelastic attenuation. The simplicity of this model allows us to isolate the effects of the sphericity on P_n and S_n geometric spreading. We use an isotropic point source for P_n simulations. The source for $S_n(SH)$ simulations is a fundamental fault vertical strike-slip source and the source for $S_n(SV)$ simulations is a dip-slip source. For all source types in our main calculations, a delta function is used as the source time function; source depth is 15 km and source strength is 10^{15} N m. Three-component synthetic ground displacements are computed at 33 locations distributed log-evenly along a linear profile from 200 km (1.8°) to 2500 km (22.5°). The Nyquist frequency of the seismograms is 20 Hz.
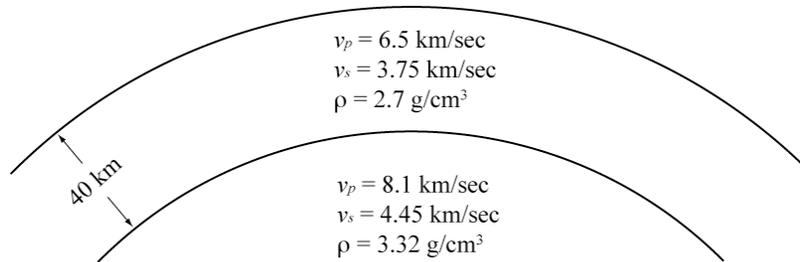

v_p = 6.5 km/sec
v_s = 3.75 km/sec
ρ = 2.7 g/cm^3

40 km

v_p = 8.1 km/sec
v_s = 4.45 km/sec
ρ = 3.32 g/cm^3

Figure 1. Base Earth model used for P_n and S_n simulations and the development of new P_n and S_n geometric-spreading models. Quality factor Q is infinite throughout the model.

We cut P_n and S_n portions of the synthetic seismograms using fixed-velocity windows. The velocities that we use to define the widths of P_n windows are 7.6 km/sec and 8.2 km/sec and those for S_n windows are 4.0 km/sec and 4.7 km/sec (Hartse, et al., 1997). The windows are centered at the peaks of the phases. We also tested a fixed-window-width method and the results remained essentially the same. We window P_n and $S_n(SV)$ from vertical-component seismograms and $S_n(SH)$ from transverse-component seismograms. After P_n and S_n seismograms are windowed, we taper the seismograms with small tapers (between 2% to 20% depending on the length of the signal relative to the window length) and Fourier transform the seismograms to obtain the amplitude spectra. We make spectral-amplitude measurements at 100 frequencies log-evenly distributed between 0.75 and 13 Hz. Amplitude at each frequency f_i is calculated by taking the average of the amplitudes between frequencies $f_i/\sqrt{2}$ and $\sqrt{2} f_i$.

To accurately assess the geometric spreading of seismic phases, the propagation medium used for the simulation should have no attenuation. However, in order to avoid a computational singularity, the reflectivity method requires a nonzero amount of attenuation for the medium. We take an asymptotic approach similar to that used by Yang (2002) to derive P_n and S_n amplitudes for an elastic model without attenuation from amplitudes calculated for a group of anelastic models. We first make 20 calculations for models that have attenuation quality factor Q log-linearly increasing from 10,000 to 100,000. For each calculation, a single Q is used for both P and S waves and for all parts of the model. Amplitudes at each frequency and each epicentral distance from these calculations are then fit by a quadratic polynomial as a function of $1/Q$. The limit of the polynomial as Q approaches infinity is taken as the amplitude at that frequency and distance for the elastic model.

P_n Modeling Results

Figure 2 plots the vertical synthetic P_n seismograms from the base-model simulation at selected epicentral distances. Q used in this simulation is 100,000. The seismograms are low-pass filtered below 10 Hz to suppress numerical noise near the Nyquist frequency. The figure reveals several interesting characteristics of P_n traveling in a spherical Earth model with constant mantle velocities. Due to the sphericity, the apparent P_n velocity is not constant, but varies with epicentral distance. As is predicted by theory (e.g., Červený and Ravindra, 1971), the pulse shape of P_n evolves from that of the impulse source at distances close to the critical distance (about 0.8° for the base model and a 15-km-deep source) to the shape of a far-field body wave, which is the time derivative of the source pulse, at farther distances. The amplitude of the phase changes in a complex manner, first decreasing and then increasing, within this distance range. At about 10° to 12°, the first pulse separates from the rest of the P_n wave packet and somewhere between 16° and 19°, a second pulse separates.
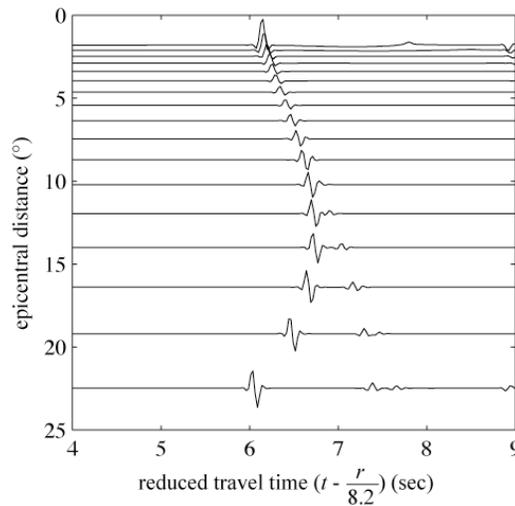
Figure 2. Synthetic P_n seismograms from base-model calculations. The seismograms are filtered below 10 Hz. Travel time is reduced by 8.2 km/sec. Only every other trace calculated is plotted to enhance clarity. r is epicentral distance in kilometers.

For high-frequency P_n at distances away from the critical distance, Červený and Ravindra (1971) offer a detailed decription of the signal behavior from ray theory. Although Červený and Ravindra (1971) describe the phenomenon for a plane-layered Earth model with positive and constant velocity gradient in the mantle, their description and conclusions are applicable to the spherical-Earth-model situation as well since the spherical model can be mapped, through the EFT, into a plane-layered model with an approximately constant velocity gradient in the uppermost mantle. Following Červený and Ravindra (1971), the P_n phase at distances between about 5° and 10° in Figure 2 can be thought of as the superposition of individual waves reflected n times ($n = 0, 1, 2, \ldots$) from the underside of the Moho. The superposed wave is termed interference head waves by Červený and Ravindra (1971) and is likened to the "whispering gallery" phenomenon by Menke and Richards (1980). As distance increases, individual components of the interference head wave start to separate from the wave packet due to their increasingly shorter path lengths compared with path lengths of the remaining waves in the wave packet. The first wave to separate is the wave that has no reflection at the Moho (the direct or diving wave). This is evidenced as the separation of the first pulse in Figure 2. The second separated pulse in the figure is the wave that is reflected once from the Moho. From ray theory, the epicentral distance at which the k-time reflected wave separates from the interference head-wave packet is (Červený and Ravindra, 1971, Eq. 6.4)

$$r_k = (2H - d)\frac{v_c}{\sqrt{v_m^2 - v_c^2}} + \left[\frac{32 v_m^3 T (1+k)^2 \left(1 + \frac{1}{2}k\right)^2}{g^2 \left(1 + \frac{2}{3}k\right)}\right]^{1/3}, \tag{4}$$

where H is crustal thickness; d is source depth; v_c is P-wave velocity of the crust; v_m is P-wave velocity at the top of the mantle; T is pulse width of the wave and g is velocity gradient (dv/dz) at the top of the mantle resulting from the EFT. From Equation 4 and for the base model, a wave with a pulse width of about 0.1 second (10-Hz) that undergoes no reflection at the Moho will separate at about 9.8° and the wave that has one reflection will separate at about 16.6°. These predictions are consistent with the synthetics in Figure 2.

Figure 3 shows the amplitude spectra of synthetic P_n at the same epicentral distances as those in Figure 2 from the Q = 100,000 computation. The figure illustrates the evolution of P_n spectrum from proportional to the source spectrum to proportional to the time derivative of the source spectrum.
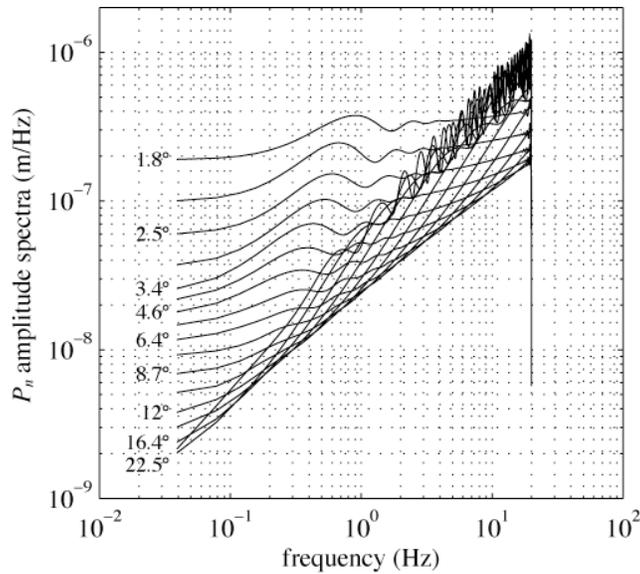
Figure 3. Amplitude spectra of P_n at the same distances as those in Figure 2. Some of the distances are marked on the left of the corresponding spectra.

As was described above, we use an asymptotic method to derive spectral amplitudes for an elastic model from amplitudes obtained using anelastic simulations. Figure 4 gives an illustration of the method. Plotted in the figure are P_n amplitudes at different frequencies measured from calculations using different quality factors. The amplitudes are computed at 22.5° epicentral distance and are normalized by the maximum amplitude in the figure. Quadratic polynomial fits of the amplitudes are plotted as solid lines. The polynomial fits are almost perfect, indicating that our approach is appropriate. Amplitudes at other distances are fit as well as those shown in Figure 4.
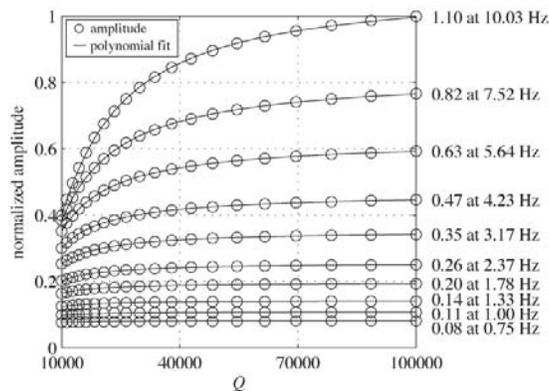

Figure 4. An illustration of how elastic results are obtained from anelastic calculations. Circles are amplitudes at 22.5° epicentral distance for different frequencies plotted against Q used in their calculations. The amplitudes are normalized by the maximum amplitude in the plot, which is the 10.03-Hz amplitude from the $Q = 100,000$ calculation. Solid lines are corresponding quadratic polynomial fits of the amplitudes. Numbers on the right are the limits of normalized amplitudes at corresponding frequencies as Q approaches infinity.

To visualize the P_n amplitude decay in a spherical Earth model, we plot 10-Hz P_n amplitudes for the base model in Figure 5. We extend the epicentral-distance range to between 135 km (1.2°) and 8000 km (71.9°) for this particular simulation in order to better depict the evolution of P_n waves. Amplitudes at distances beyond about 20° are measured from the direct wave that has been completely separated from the interference head waves. The

amplitudes are corrected for the free-surface effect, which is only important at teleseismic distances. Also plotted in the figure are the amplitude decay of a conical head wave in a plane one-layer-over-half-space model (Aki and Richards, 2002; Eq. 6.26) and the amplitude decay of infinite-frequency direct wave in a spherical Earth model from ray tracing. At distances close to the critical distance, P_n geometric spreading behaves like that of a conical head wave. As distance increases, P_n spreading starts to deviate from that of the head wave and at about 5°, P_n amplitudes begin to increase. As was mentioned before, 10-Hz direct-wave energy would separate from the rest of the interference head wave at about 10°. It seems from the figure that this separation is manifested in a change in the smoothness of the P_n amplitude variation followed by a reduced rate of amplitude increase. In the range beyond the critical distance and before the direct-wave separation, P_n evolves from a wave similar to a conical head wave to the interference head wave, which is a superposition of multiple waves reflected from the Moho. As the epicentral distance approaches teleseismic distances, the direct-wave spreading approaches that of the infinite-frequency wave from ray tracing results, as is expected. The direct wave dominates the whole P_n wave packet at long distances. We do not see significant difference between spectral amplitudes obtained by windowing the whole P_n wave packet and those obtained by just windowing the direct wave after its separation from the packet. This is consistent with theoretical predictions (Červený and Ravindra, 1971).
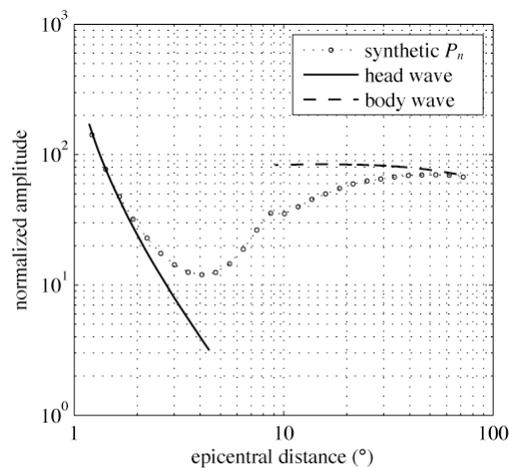

Figure 5. 10-Hz synthetic P_n amplitude decay in a spherical Earth model with constant mantle velocities. The solid line depicts the theoretical amplitude decay of a conical head wave in a plane one-layer-over-half-space Earth model. The dashed line is the amplitude decay of infinite-frequency direct wave in a spherical homogeneous Earth model from ray-tracing calculations.

P_n geometric spreading in a spherical Earth model is not only different from that of a head wave as is shown in Figure 5, but also frequency dependent. Figure 6 shows the P_n amplitude-variation surface as a function of distance and frequency for the base model. The strong frequency dependence of the amplitudes is apparent. Amplitudes at higher frequencies are affected more by the sphericity than are lower-frequency amplitudes. The separation distance of the direct wave from the interference head waves becomes shorter as frequency becomes higher (Equation 4).
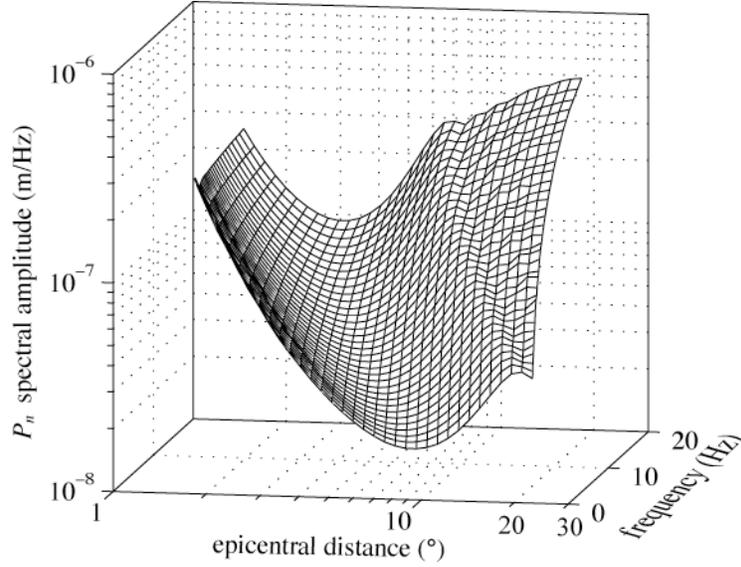
Figure 6. Synthetic P_n amplitudes as a function of epicentral distance and frequency.

A New P_n Geometric-Spreading Representation for a Spherical Earth Model

Figures 5 and 6 illustrate that a frequency-independent, power-law model cannot accurately represent P_n geometric spreading in a spherical Earth model. Such a representation would plot as a straight line in Figure 5, which is clearly inappropriate for modeling P_n geometric spreading over a wide distance range. In addition, a power-law model with constant exponent does not take into account the frequency dependence of P_n spreading shown in Figure 6. Based on the P_n amplitude-decay behavior shown in Figures 5 and 6, we propose a new empirical P_n geometric-spreading model that fits the synthetic data much better and that also results in more reasonable anelastic-attenuation estimates from observed data, as we will discuss in more detail in the next section.

The amplitude spectrum of P_n can be parameterized as

$$A(r,\theta,f) = K(f)M_0R(\theta)G(r,f)\exp\left(-\frac{\pi f}{Q(f)v}r\right)S(f) \tag{5}$$

with the new geometric-spreading model expressed as

$$G(r,f) = \frac{10^{n_3(f)}}{r_0}\left(\frac{r_0}{r}\right)^{n_1(f)\log\left(\frac{r_0}{r}\right)+n_2(f)} \quad (r_0 = 1 \text{ km}) \tag{6}$$

and

$$n_i(f) = n_{i1}\left[\log\left(\frac{f}{f_0}\right)\right]^2 + n_{i2}\log\left(\frac{f}{f_0}\right) + n_{i3} \quad (i = 1, 2, 3; f_0 = 1 \text{ Hz}). \tag{7}$$

In Equation 5, K is a frequency-dependent scaling factor; M_0 is source moment; R is source radiation pattern; Q is P_n quality factor; v is P_n velocity; S is receiver site response; r is epicentral distance; θ is azimuth angle and f is frequency. r_0 and f_0 are included in Equations 6 and 7 in order for the new model to have the same dimension as standard power-law models (e.g., Street et al., 1975; Sereno et al., 1988). The main differences between the new geometric-spreading model (Equations 6 and 7) and the standard frequency-independent power-law model are the addition of the first term in the exponent and the frequency dependence of parameters n_i. In the logarithm domain, the new model is a quadratic function of log-distance, whereas the power-law model is linear. The reason for choosing a log-quadratic function is to keep the parameterization as simple as possible while providing a good fit to the synthetics. The adoption of a quadratic functional form for n_i (Equation 7) is based on the behavior of n_i versus frequency obtained by fitting Equation 6 to synthetic P_n amplitudes at individual frequencies.

If we take common logarithm of Equation 6, substitute Equation 7 into the result and let r_0 and f_0 equal one, we obtain

$$\log[G(r,f)] = n_{11}(\log f)^2(\log r)^2 + n_{12}\log f(\log r)^2 + n_{13}(\log r)^2$$
$$-n_{21}(\log f)^2\log r - n_{22}\log f\log r - n_{23}\log r \qquad , \qquad (8)$$
$$+n_{31}(\log f)^2 + n_{32}\log f + n_{33}$$

where r is in kilometers and f is in hertz. To derive coefficients n_{ij}, we fit Equation 8 to synthetic P_n amplitudes shown in Figure 6 in a least-squares sense. P_n amplitudes are corrected for M_0 used in the simulation (10^{15} N m) and K before the fitting. Since the source that we use in the simulation has a flat spectrum, K is frequency independent. We use $K = (4\pi\rho v^3)^{-1}$ (Denny and Johnson, 1991), where ρ is density and v is P-wave velocity of the source region. Source radiation and site response are unity. We use P_n amplitudes at epicentral distances beyond 300 km (2.7°) and before the start of the direct-wave separation to fit the model. We use 300 km as the lower distance limit because reliable P_n observations are typically made at some distances beyond the P_g crossover distance (~200 km). The choice of 300 km is also to avoid possible long-period numeric-noise contamination at short distances, as is indicated in Figure 6. The upper distance limits are based on the observation that within these distances, P_n is the result of the interference of all of its components including the direct wave. At larger distances, the direct wave separates from the rest of the wave packet and the characteristics of P_n become different. The P_n amplitude decay within the defined distance range also has a smooth pattern and thus is easier to fit by a simple mathematical model. The upper distance limits vary from 7.3° to 17.3° for the frequency range between 13 and 0.75 Hz. Within the specified distance limits, the new spreading model is applicable. Since at about 15°, P_n in the real Earth is overtaken by upper-mantle triplications resulting from reflections and refractions at 410-km and 660-km discontinuities and is no longer the first arrival, P_n is usually used within the distance range where the new spreading model is valid for frequencies below about 2 Hz. For higher frequencies, the range-of-applicability of the new model is shorter, but observationally high-frequency signals are generally only detectable above the noise level at shorter distances. Coefficients n_{ij} ($i = 1, 2, 3; j = 1, 2, 3$) from the fitting are listed in Table 1. The inclusion of r_0 and f_0 in the model also guarantees that even though the values of the coefficients are derived using Equation 8 with r in kilometers and f in hertz, they are valid for r and f in any units as long as r_0 and f_0 are converted accordingly.

Table 1 Coefficients of the new P_n geometric-spreading model

n_{11}	n_{12}	n_{13}	n_{21}	n_{22}	n_{23}	n_{31}	n_{32}	n_{33}
-0.217	1.79	3.16	-1.94	8.43	18.6	-3.39	9.94	20.7

Application to Observed Data

The key value of any mathematical model of the physical world is for the model to be able to provide physically reasonable descriptions of observed data. To test the validity and usefulness of the new P_n geometric-spreading model and the associated choice of a constant-velocity mantle lid structure, we correct a set of observed P_n spectral amplitudes for geometric spreading with the new model and estimate the average medium attenuation. We then compare the results with those published in the literature.

We represent observed P_n amplitudes by Equation 5. For the purpose of testing the new P_n geometric-spreading model, we simplify Equation 5 by assuming that site response is unity for all stations and source radiation patterns can be ignored. We presume that errors introduced by these simplifications are random and should not affect average-attenuation estimates systematically. With known or estimated source moments, an assumed scaling factor K and a P_n geometric-spreading model, we can estimate the average attenuation quality factor at each frequency by least-squares fitting the logarithm of source and geometric-spreading corrected spectral amplitudes as a function of epicentral distance.

The observed P_n amplitudes are measured on vertical-component ground-displacement data recorded by stations in and around China and in southern Europe for events in the same region. The same windowing method as the method we employ to measure the synthetic P_n amplitudes is used. Analyst picks reported in global catalogs (ISC, EDR, REB, EHB, etc.) are used to center the P_n windows. We derive source moments from body-wave magnitudes (m_b). We only use amplitudes from events with m_b equal to or smaller than 6 to avoid magnitude saturation. We use a

simplified version of the scaling factor K expressed as $K(f) = \{4\pi\rho v^3[1+(f/f_c)^2]\}^{-1}$ using crustal P-wave velocity and density of the base Earth model as v and ρ. Source corner frequency f_c is calculated from source moment using the relationship $\log M_0 = 17.08 - 3.24\log f_c$ derived by Xie and Patton (1999) from P_n amplitude data recorded in central Asia. For comparison, we use both the new P_n geometric-spreading model and the power-law model with two different exponents, -1.1 (Walter and Taylor, 2002) and -1.3, in the attenuation estimation. When the new spreading model is used, we limit the epicentral distances of the amplitudes used in the estimation to within the distance range where the model is valid. For power-law model corrections, we use amplitudes between 300 km (2.7°) and 1668 km (15°). Attenuation is estimated at 0.75, 1.0, 2.0, 4.0 and 6.0 Hz. The new spreading model is used in the correction. Although the amplitudes show a large scatter, a linear decay trend due to realistic values of medium attenuation is discernable.

Table 2 lists estimated average quality factors using different geometric-spreading corrections from observed P_n amplitudes. Using the power-law spreading model results in some negative values at low frequencies. At high frequencies, the power-law model yields estimates that range from over 1000 to over 5000. On the other hand, Q estimates using the new spreading model are positive and below 700 at all frequencies. These values can be compared with published P-wave quality factors in the mantle lid, as we discuss below.

Table 2 Average P_n quality factor estimated using different geometric-spreading models

	data frequency (Hz)				
	0.75	1.0	2.0	4.0	6.0
new model	440	338	312	557	678
power-law model 1[*]	-1669	9241	1206	2204	3450
power-law model 2[**]	-734	-2153	1850	3260	5246

[*] model with exponent of -1.1

[**] model with exponent of -1.3

Using theory, observed body-wave spectra and waveform modeling, Lundquist and Cormier (1980) derive generic absorption-band P-wave Q models for the mantle. The Q values of these models range from about 100 to 500 for frequencies between 0.7 Hz and 6.0 Hz in the depth range of 45 to 200 km. In their paper, Lundquist and Cormier (1980) also cites results of some other Q studies that use free-oscillation data, long-period surface waves and high-frequency (1-5 Hz) body waves. The frequency-independent P-wave Q models from these studies have values from about 100 to 250 for depths between 50 and 150 km. Der et al. (1986) construct a P-wave Q model for the Eurasian Shield using a large set of teleseismic body waves. Their model has values between about 350 and 900 for frequencies between 0.3 and 10 Hz at depths between 100 and 200 km. Above 100 km, Q values increase to between 600 and 1500 for the same frequency range.

More recently, some studies make direct P_n Q estimations. Sereno *et al.* (1988) and Sereno (1990) obtain P_n Q models for Scandinavia and eastern Kazakhstan respectively by inverting broadband P_n spectra.
The 0.75- to 6-Hz P_n Q values that they estimated are between 283 and 768 for Scandinavia and between 260 and 735 for eastern Kazakhstan. Although Sereno et al. (1988) and Sereno (1990) assume a power-law P_n geometric-spreading model with an exponent of -1.3, their P_n Q estimates are more in line with the average P_n Q estimates that we obtain using the new P_n spreading model than with those from power-law model corrections (Table 2). A possible explanation for this observation is that the majority of their data are recorded within 1000-km epicentral distance. At short distances, the power-law spreading model has a gentler slope than the new spreading model does and therefore would yield smaller Q estimates from short-distance data. However, for a broader distance range such as the distance range that our dataset covers, the power-law model yields larger, sometimes negative, Q estimates because of the steeper slope of the model at long distances. The implication is that if a power-law P_n spreading model with a specific exponent is used, it will only be applicable as an approximation in a limited distance range and models with different exponents are needed for different distance ranges. Our parameterization remedies this failing.

Comparing Q values in Table 2 with those published in the literature, we conclude that the new P_n geometric-spreading model yields Q estimates that are generally consistent with published results over the broad region of Eurasia. The Q estimates with power-law model corrections, on the other hand, have values that are either negative or seem to be too large. It should be noted that Q values estimated in this fashion represent only the average P_n attenuation behavior over the broad region of Eurasia. They may not be accurate for any particular region due to the deviation of the uppermost-mantle velocity structure, including any non-zero mantle lid velocity gradient or lateral heterogeneity, from the constant-velocity structure that we use to develop the geometric-spreading model. The fact that we obtain reasonable Q values for data spanning a large distance range demonstrates that our reference model at least provides reasonable average behavior without any peculiarities such as negative Q values.

S_n Simulations

In addition to simulating P_n propagation in a spherical Earth model, we also simulate S_n propagation in the same base model. Except for different source types and different slowness integration limits, other modeling parameters in the S_n simulation are kept the same as those used in the P_n simulation. The behavior of S_n in a spherical Earth model is very similar to the behavior of P_n waves. The only difference is that the separation of individual waves from the interference wave packet occurs at shorter distances for S_n. This difference can be predicted using Equation 4, although the equation was originally derived only for P_n waves. $S_n(SH)$ spectral amplitudes also form a surface with a shape similar to that of the P_n amplitude surface shown in Figure 6.

Because of the similarities between P_n and S_n propagation in a spherical Earth model with constant mantle velocities, we propose an S_n geometric-spreading model that has the same functional form as that of the new P_n spreading model (Equations 6 and 7). We derive the values of the coefficients n_{ij} by fitting synthetic $S_n(SH)$ amplitudes. $S_n(SV)$ amplitudes are severely contaminated by P-wave energy up to 1000 km, and thus are not suitable for fitting. Beyond 1000 km, $S_n(SV)$ and $S_n(SH)$ amplitudes decay similarly. It suggests that the S_n spreading model developed by fitting $S_n(SH)$ amplitudes is also suitable for describing $S_n(SV)$ geometric spreading.

We correct synthetic $S_n(SH)$ amplitudes for source moment, source radiation pattern, and the scaling factor K before the fitting. We use $K = (4\pi\rho v^3)^{-1}$, but now v is S-wave velocity of the crust. We again set the lower-distance limit to 300 km (2.7°) for amplitudes used in the fitting. The upper distance limits are from 6.2° to 14.4° for frequencies from 13 Hz to 0.75 Hz. The limits set the distance range within which the S_n spreading model is valid. Table 3 lists the coefficients n_{ij} for the S_n geometric-spreading model from the fitting.

Table 3 Coefficients of the new $S_n(SH)$ geometric-spreading model

n_{11}	n_{12}	n_{13}	n_{21}	n_{22}	n_{23}	n_{31}	n_{32}	n_{33}
-0.347	2.16	3.54	-2.69	10.1	20.4	-4.38	11.7	23.1

CONCLUSIONS AND RECOMMENDATIONS

The new P_n and S_n geometric-spreading models are useful in common situations where only simple velocity models with uppermost-mantle structure represented as constant-velocity half space or a stack of constant velocity layers are available. If the mantle-lid velocity gradient is well resolved in a given region, which is sometimes the case, simulations for that gradient can be performed to obtain appropriate geometric-spreading corrections. Since the effect of sphericity is equivalent to the effect of a positive velocity gradient in a plane-layered model, we anticipate that the functional form of our geometric-spreading models will remain the same for Earth models in which an effective (physical plus effects of the sphericity) positive velocity gradient exists. Only the coefficients will differ. Of course, any Q determinations will trade-off directly with errors due to having the wrong velocity model, and if one can determine specific structural parameters they should be used to make specific geometric spreading terms.

Quantifying the effects of specific mantle-lid velocity gradients, Moho irregularity and lateral velocity heterogeneity in the uppermost mantle on P_n and S_n geometric spreading through 2D and 3D numerical modeling will be the subject of a separate study. It is reasonable to assume that except for the case of different lid velocity gradients, many effects will contribute primarily to scatter around the fundamental behavior of our geometric-spreading models.

REFERENCES

Aki, K., and P. G. Richards (2002). *Quantitative Seismology*, 2nd edition, University Science Books, Sausalito, California.

Červený, V., and R. Ravindra (1971). *Theory of Seismic Head Waves*, University of Toronto Press, Toronto.

Chapman, C. H. (1973). The Earth flattening transformation in body wave theory, *Geophys. J. R. astr. Soc.* 35: 55–70.

Denny, M. D., and L. R. Johnson (1991). The explosion seismic source function: models and scaling laws reviewed, in *Explosion Source Phenomenology*, S. R. Taylor, H. J. Patton, and P. G. Richards (Editors), American Geophysical Union, Washington, DC, 1–24.

Der, Z. A., A. C. Lees, and V. C. Cormier (1986). Frequency dependence of Q in the mantle underlying the shield areas of Eurasia. III. The Q model, *Geophys. J. Int.* 87: 1103–1112.

Hartse, H. E., S. R. Taylor, W. S. Phillips, and G. E. Randall (1997). A preliminary study of regional seismic discrimination in central Asia with emphasis on western China, *Bull. Seism. Soc. Am.* 87: 551–568.

Lundquist, G. M., and V. C. Cormier (1980). Constraints on the absorption band model of Q, *J. Geophys. Res.* 85: 5244–5256.

Menke, W. H., and P. G. Richards (1980). Crust-mantle whispering gallery phases: a deterministic model of teleseismic P_n wave propagation, *J. Geophys. Res.* 85: 5416–5422.

Müller, G. (1977). Earth-flattening approximation for body waves derived from geometric ray theory—improvements, corrections and range of applicability, *J. Geophys.* 42: 429–436.

Sereno, T. J., and J. W. Given (1990). *P_n* attenuation for a spherically symmetric Earth model, *Geophys. Res. Lett.* 17: 1141–1144.

Sereno, T. J., S. R. Bratt, and T. C. Bache (1988). Simultaneous inversion of regional wave spectra for attenuation and seismic moment in Scandinavia, *J. Geophys. Res.* 93: 2019–2035.

Sereno, T. J. (1990). Frequency-dependent attenuation in eastern Kazakhstan and implications for seismic detection threshold in the Soviet Union, *Bull. Seism. Soc. Am.* 80: 2089-2105.

Street, R. L., R. B. Herrmann and O. W. Nuttli (1975). Spectral characteristics of the L_g wave generated by central United States earthquakes, *Geophys. J. R. astr. Soc.* 41**:** 51–63.

Walter, W. R., and S. R. Taylor (2002). A revised magnitude and distance amplitude correction (MDAC2) procedure for regional seismic discriminants: theory and testing at NTS, Lawrence Livermore National Laboratory, UCRL-ID-146882, pp. 13.

Xie, X.-B., and T. Lay (1994). The excitation of Lg waves by explosions: A finite-difference investigation, *Bull. Seism. Soc. Am.* 84: 324–342.

Xie, J., and H. J. Patton (1999). Regional phase excitation and propagation in the Lop Nor region of central Asia and implications for *P*/*Lg* discriminants, *J. Geophys. Res.* 104: 941–954.

Yang, X. (2002). A numerical investigation of L_g geometric spreading, *Bull. Seism. Soc. Am.* 92: 3067–3079.